Nano-Micro Letters
e-ISSN 2150-5551
CN 31-2103/TB
ARTICLE
https://doi.org/10.1007/s40820-025-02045-z

Cite as
Nano-Micro Lett.
(2026) 18:201

Received: 13 September 2025
Accepted: 7 December 2025

Textured and Hierarchically Porous Hematite Photoanode for Efficient Hydrogen Production via Photoelectrochemical Hydrazine Oxidation

Runfa Tan[1,2], Yoo Jae Jeong[1,3], Hyun Soo Han[6], Samadhan Kapse[1,2], Seong Sik Shin[4,5], Xiaolin Zheng[6] ✉, In Sun Cho[1,2] ✉

ARTICLE HIGHIGHTS

- A multi-cycle growth and flame annealing strategy was developed to construct textured and hierarchically porous Ti-doped hematite (tp-Fe_2O_3) photoanodes with enhanced charge transport and surface kinetics.
- The hydrazine oxidation reaction was introduced as a fast and thermodynamically favorable alternative to the oxygen evolution reaction, enabling the simultaneous production of hydrogen and the remediation of toxic hydrazine.
- The tp-Fe_2O_3-based bias-free photovoltaic-photoelectrochemical tandem device achieved a record solar-to-hydrogen efficiency of 8.7%, demonstrating excellent stability and scalability for sustainable solar fuel generation.

ABSTRACT The performance of hematite (α-Fe_2O_3) photoanodes for photoelectrochemical (PEC) water splitting has been limited to around 2–5 mA cm^{-2} under standard conditions due to their short hole diffusion length and sluggish oxygen evolution reaction kinetics. This work overcomes those challenges through a synergistic strategy that co-designs the hematite architecture and the surface reaction pathway. We introduce a textured and hierarchically porous Ti-doped Fe_2O_3 (tp-Fe_2O_3) photoanode, synthesized via multi-cycle growth and flame annealing method. This unique architecture features a high texture (110), enlarged surface area, and hierarchically porous structure, which enable significantly enhanced bulk charge transport and interfacial charge transfer compared to typical nanorod Ti-doped Fe_2O_3 (nr-Fe_2O_3). As a result, the tp-Fe_2O_3 photoanode achieves a photocurrent density of 3.1 mA cm^{-2} at 1.23 V vs. RHE with exceptional stability over 105 h, notably without any co-catalyst. By replacing the OER with the hydrazine oxidation reaction, the photocurrent further reaches a record-high level of 7.1 mA cm^{-2} at 1.23 V_{RHE}. Finally, when we integrate the tp-Fe_2O_3 with a commercial Si solar cell, it achieves a solar-to-hydrogen efficiency of 8.7%—the highest reported value for any Fe_2O_3-based PV-tandem system. This work provides critical insights into rational Fe_2O_3 photoanode design and highlights the potential of hydrazine as an efficient alternative anodic reaction, enabling waste valorization.

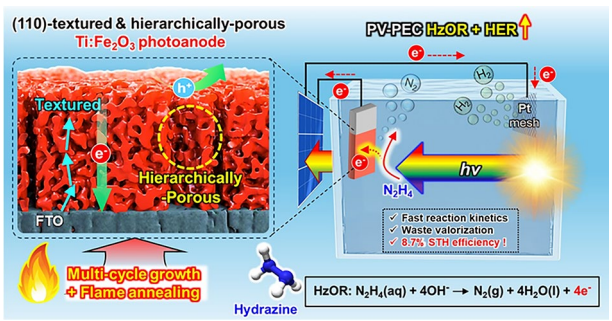

KEYWORDS Hematite; Hierarchically porous; Texture; Hydrazine oxidation reaction; Solar-to-hydrogen

Runfa Tan and Yoo Jae Jeong have contributed equally to this work.

✉ Xiaolin Zheng, xlzheng@stanford.edu; In Sun Cho, insuncho@ajou.ac.kr
[1] Department of Materials Science & Engineering, Ajou University, Suwon 16499, Republic of Korea
[2] Department of Energy Systems Research, Ajou University, Suwon 16499, Republic of Korea
[3] Materials Science and Engineering Program, University of Colorado Boulder, Boulder, CO 80303, USA
[4] SKKU Advanced Institute of Nanotechnology (SAINT) and Department of Nanoengineering, Sungkyunkwan University, Suwon 16419, Republic of Korea
[5] Department of Energy Science, Sungkyunkwan University, Suwon 16419, Republic of Korea
[6] Department of Mechanical Engineering, Stanford University, Stanford, CA 94305, USA

Published online: 08 January 2026

1 Introduction

Photoelectrochemical (PEC) water splitting, *i.e.*, direct conversion of sunlight into hydrogen [1–3], faces two major challenges: a lack of suitable photoanode materials and the sluggish kinetics of the oxygen evolution reaction (OER). These limitations result in low photocurrent densities and low solar-to-hydrogen (STH) conversion efficiency of PEC systems [4]. To overcome these challenges, prior research has focused on two complementary strategies: (i) rational design and optimization of photoanode materials for better charge separation and transport [5–7], and (ii) utilizing alternative oxidation reactions (AORs) that have faster kinetics and lower overpotentials than OER [8]. Using AORs not only enhances hydrogen production but also enables the generation of valuable chemicals or the degradation of hazardous pollutants, thereby contributing to environmental remediation and the circular utilization of resources [9–19].

In terms of potential photoanode candidates for PEC systems, hematite (α-Fe_2O_3) remains a stronger contender due to its abundance in the Earth's crust, low cost, excellent chemical stability, and a suitable bandgap (~ 2.1 eV) for efficient visible light absorption [20]. However, Fe_2O_3 possesses intrinsic drawbacks, including an extremely short hole diffusion length (~ 2–4 nm), low electrical conductivity, and significant charge recombination in both the bulk and at the surface [21], so the photocurrent densities of bare Fe_2O_3 photoanodes typically are below a few mA cm^{-2} at 1.23 V vs. the reversible hydrogen electrode (RHE, V_{RHE}) under OER conditions. Although numerous strategies, such as elemental doping, co-catalyst loading, junction formation, and morphological engineering [22–26], have been explored to overcome these limitations, the photocurrent densities achieved by a single hematite photoanode still generally limited to 2–5 mA cm^{-2} at 1.23 V_{RHE}, which is still far below the theoretical maximum of 12.6 mA cm^{-2} evaluated based on light absorption. Device-level approaches, such as parallel stacking of multiple transparent hematite photoanodes, have achieved photocurrents approaching ~ 10 mA cm^{-2} under standard conditions [27]; however, these configurations do not represent the intrinsic performance of a single hematite photoanode.

In the context of AORs, only a limited number of studies have explored their application on Fe_2O_3 photoanodes, including the oxidation of ethylene glycol, glucose, methanol, and ethanol to replace the sluggish OER [28–31]. Among these, L-cysteine oxidation has shown the highest photocurrent density, reaching up to 4.6 mA cm^{-2} at 1.23 V_{RHE} using a Ti/Si dual-doped porous nanorod Fe_2O_3 [32]. However, this value remains significantly below the theoretical maximum value. Moreover, most organic AORs involve complex multi-electron pathways that generate various byproducts, often causing catalyst deactivation, surface fouling, and poor long-term stability. Hydrazine (N_2H_4), widely used as a high-energy propellant in aerospace and as a reducing agent in pharmaceutical synthesis, is also highly toxic and carcinogenic; its uncontrolled release into industrial wastewater poses serious environmental risks [33]. Conventional removal of hydrazine waste typically relies on chemical oxidation, which consumes additional reagents and may pose safety concerns. In contrast, hydrazine undergoes a clean and rapid oxidation reaction with minimal formation of byproducts. Therefore, integrating the hydrazine oxidation reaction (HzOR) into PEC systems for hydrogen production offers a dual benefit: (i) providing a thermodynamically and kinetically favorable alternative to the sluggish OER, and (ii) enabling simultaneous H_2 generation and environmental remediation. These attributes make HzOR an attractive strategy for enhancing the PEC efficiency of Fe_2O_3 photoanodes, especially when combined with structural and electronic optimizations.

In this study, we demonstrate a dual strategy to enhance the PEC performance of Fe_2O_3 photoanode: (i) structural engineering to improve charge dynamics, and (ii) employing hydrazine oxidation reaction (HzOR) as a kinetically favorable alternative to the sluggish OER. For structural engineering, we developed a novel multi-cycle growth and flame annealing (MGFA) method to fabricate textured, hierarchically porous hematite (tp-Fe_2O_3) photoanodes, overcoming the limitations of typical nanorod-structured Fe_2O_3 (nr-Fe_2O_3). The tp-Fe_2O_3 exhibits several key features, including an enhanced (110) crystallographic texture, a uniform depth profile of Ti dopants, and a hierarchically porous architecture with an increased surface area. These structural and compositional modifications significantly enhance charge carrier dynamics, leading to efficient bulk charge transport and interfacial charge transfer. As a result, the tp-Fe_2O_3 photoanode exhibits excellent PEC performance, achieving a

 https://doi.org/10.1007/s40820-025-02045-z

stable photocurrent density of 3.1 mA cm^{-2} at 1.23 V_{RHE} for OER without any co-catalysts. Notably, by replacing OER with HzOR, a record-high photocurrent density of 7.1 mA cm^{-2} is achieved at the same potential. Furthermore, integration of the tp-Fe_2O_3 into a bias-free photovoltaic-photoelectrochemical (PV-PEC) tandem system coupling HzOR with hydrogen evolution reaction (HER) results in a solar-to-hydrogen (STH) efficiency of 8.7%—the highest reported for Fe_2O_3-based tandem devices. This work not only provides critical insights into the rational design of high-performance Fe_2O_3 photoanodes but also highlights the significant potential of hydrazine oxidation as a sustainable, efficient alternative pathway for solar-driven H_2 production.

2 Experimental Section

2.1 Synthesis of Textured, Hierarchically Porous Hematite (tp-Fe_2O_3)

We synthesized tp-Fe_2O_3 photoanodes using a MGFA method. Initially, a precursor solution containing 10 mmol of $FeCl_3{\cdot}6H_2O$, 15 mmol of urea, 1 mmol of $TiCl_3$, and 100 mL of deionized water was prepared in a Pyrex glass bottle. Cleaned FTO substrates (1.5 cm × 2.5 cm) were vertically suspended in this solution using Teflon threads and heated at 100 °C for 6 h in a sealed glass bottle to form a Ti-doped FeOOH. Subsequently, multi-cycle growth was performed under the same chemical conditions, but with a shortened reaction time of 2 h per cycle. The growth cycle was repeated six times to optimize the film thickness and hierarchical morphology. The resulting Ti-doped FeOOH films with multi-branched structure were then subjected to flame annealing using a premixed CH_4/air flame (equivalence ratio $\Phi = 0.7$) for 5 min. The flame annealing process, characterized by an ultrafast heating rate (> 100 °C s^{-1}), enables rapid phase transition and crystallization of the Ti-doped FeOOH multi-branched nanorods into Ti-doped Fe_2O_3 and dopant activation without severe damage to underlying FTO substrates [34, 35]. The ultrafast heating rate and short duration suppress grain growth. Notably, the flame annealing preserved the multi-branched morphology and induced oriented crystallization of the branches along the core nanorods, promoting a hierarchically porous and (110)-textured structure via epitaxial crystallization from the underlying 1D framework.

2.2 Synthesis of Typical Nanorod-Structured Hematite (nr-Fe_2O_3)

We prepared the control nr-Fe_2O_3 photoanodes by a single-cycle growth followed by ex situ Ti doping [36]. A precursor solution identical to that used for tp-Fe_2O_3, except without Ti addition, was prepared, and the FTO substrates were immersed vertically and heated at 100 °C for 6 h to grow vertically aligned FeOOH nanorods. After drying, Ti doping was performed by dip-coating the FeOOH nanorod film with a 0.02 M $Ti(OBu)_4$ solution in 2-methoxyethanol. The films were dried at 80 °C in air and then annealed using the same flame treatment protocol as above to obtain a Ti-doped Fe_2O_3 nanorod structure.

2.3 Material Characterization

The crystal structures of the samples were characterized by X-ray diffraction (XRD, Rigaku D/MAX-Ultima III) using Cu Kα radiation (λ = 1.5406 Å). Raman spectra were collected using a confocal Raman microscope (WITec alpha300 R) with a 532 nm laser. Surface morphology and film thickness were examined using field-emission scanning electron microscopy (FE-SEM, JEOL JSM-IT500HR). The detailed internal microstructure and porosity were analyzed using transmission electron microscopy (TEM, FEI Titan 80–300 kV) and energy-dispersive X-ray spectroscopy (EDS). The specific surface area and Barrett–Joyner–Halenda (BJH) pore size distribution were evaluated using Brunauer–Emmett–Teller (BET) analysis using N_2 adsorption–desorption isotherms (Micromeritics ASAP 2020 Plus). UV–Vis absorption spectra were obtained with a Shimadzu UV-2600i spectrophotometer. Wettability was assessed using a contact angle goniometer (Theta Lite TL101). Surface potential distributions under dark and illuminated conditions were examined via Kelvin probe force microscopy (KPFM, Asylum MFP-30). Chemical states and dopant profiles were analyzed using X-ray photoelectron spectroscopy (XPS, Thermo ESCALAB 250Xi), with Ar^+ ion etching employed for depth profiling.

2.4 Photoelectrochemical and Electrochemical Measurements

PEC measurements were conducted in a three-electrode configuration under AM 1.5G illumination (1 sun, 100 mW

cm^{-2}). A 1 M NaOH (pH 13.6) solution was used as the electrolyte for water oxidation. For the HzOR, 0.1 M N_2H_4 was added to the 1 M NaOH electrolyte. J–V curves were obtained under dark and 1 sun illumination by linear sweep voltammetry (LSV) at a scan rate of 50 mV s^{-1}. Temperature-dependent J–V measurements were performed to derive activation energies based on Arrhenius plots of ln(J) vs. 1/T. Mott–Schottky plots were measured at 1 kHz in the dark to determine the flat-band potential and donor density. Electrochemical impedance spectroscopy (EIS) was performed under potentiostatic conditions over a frequency range of 0.1 Hz to 1 MHz. An equivalent circuit model was employed to extract parameters, including R_{bulk}, C_{bulk}, R_{ct}, and C_{trap}. The electrochemically active surface area (ECSA) was estimated from the linear relationship between the capacitive current and the scan rate under dark conditions. Charge transport and transfer efficiencies of the Fe_2O_3 photoanode were evaluated as a function of applied potential using H_2O_2 as a sacrificial agent. For tandem PV-PEC measurements, a commercial crystalline Si solar cell (Ningbo Aike Electronics Technology Co., Ltd.) was coupled to the PEC cell in a two-electrode configuration. Both devices were simultaneously illuminated to evaluate the feasibility of bias-free H_2 production via hydrazine oxidation.

3 Results and Discussion

3.1 Synthesis and Structural Characterization of tp-Fe_2O_3

Figure 1a, b provides a schematic representation of the synthetic process and structural features of textured and hierarchically porous Ti-doped Fe_2O_3 (tp-Fe_2O_3) obtained via a multi-cycle growth and flame annealing (MGFA) method. Detailed flame setup and method are shown in Figs. S1 and S2. For comparison, the typical nanorod-structured Ti-doped Fe_2O_3 (nr-Fe_2O_3) was also synthesized (Figs. S3–S5).

Notably, this multi-cycle growth (1–8 cycles, Fig. S6) ensures adequate film thickness and promotes the formation of a cauliflower-like, branched FeOOH morphology with high structural complexity (Fig. S7). The final step involves high-temperature flame annealing under fuel-lean conditions (oxidizing atmosphere) for 5 min, which induces a phase transition and fusion of the branched nanorods into a unique, textured, and hierarchically porous Fe_2O_3 (Figs. S8 and S9). A 5 min oxidation flame annealing was identified as optimal, providing the highest porosity and smallest lateral grain size while minimizing FTO substrate damage and achieving the highest photocurrent density for water oxidation (Figs. S10 and S11). To identify the impact of flame annealing, the multi-cycle-grown FeOOH was subjected to conventional furnace annealing for the same duration (5 min). Unlike the flame-treated sample, the conventional furnace-annealed Fe_2O_3 exhibited significant aggregation, enlarged grain size, and diminished porosity, resulting in inferior PEC performance (Fig. S12). Therefore, flame annealing is advantageous for constructing a hierarchically porous and network structure of Fe_2O_3, which is attributed to its distinct heat transfer mechanisms (directional heat transfer, high heat flux, high temperature, and rapid ramping rate) [36–38].

Figure 1c, d presents top-view and cross-sectional SEM images of the synthesized tp-Fe_2O_3 photoanode, respectively. The top-view image (Fig. 1c) reveals a porous and interconnected three-dimensional (3D) network morphology that has a large porosity and surface area. The cross-sectional SEM image (Fig. 1d) displays a well-defined 3D morphology and intimate, uniform deposition on the FTO substrate. Notably, the intimate contact between the tp-Fe_2O_3 photoanode and the FTO substrate ensures strong adhesion and good electrical connectivity, which is essential for efficient and stable PEC performance [39, 40]. As shown in Fig. 1e, all three elements (Fe, Ti, and O) are uniformly distributed throughout the nanostructure, indicating homogeneous doping and consistent growth across the film.

Figure 1f shows a cross-sectional view of a TEM image of tp-Fe_2O_3, revealing the presence of abundant pores throughout the structure. A higher magnification view further confirms the existence of both nano- and mesopores, highlighting the multi-scale porous architecture (Fig. S13). The hierarchically porous network structure indicates a high degree of structural complexity, which facilitates electrolyte penetration and increases the active surface area, beneficial for the PEC performance [41–43].

Figure 1g presents high-resolution TEM (HR-TEM) images of three selected regions—top surface (A), middle bulk (B), and bottom interface (C)—of the tp-Fe_2O_3 photoanode, as marked in Fig. 1f. The corresponding fast Fourier transform (FFT) patterns confirm the high crystallinity and phase purity of Fe_2O_3 throughout the film. The observed lattice spacings of 0.16, 0.27, and 0.36 nm correspond to the (122), (104), and (012) planes of α-Fe_2O_3, respectively,

 https://doi.org/10.1007/s40820-025-02045-z

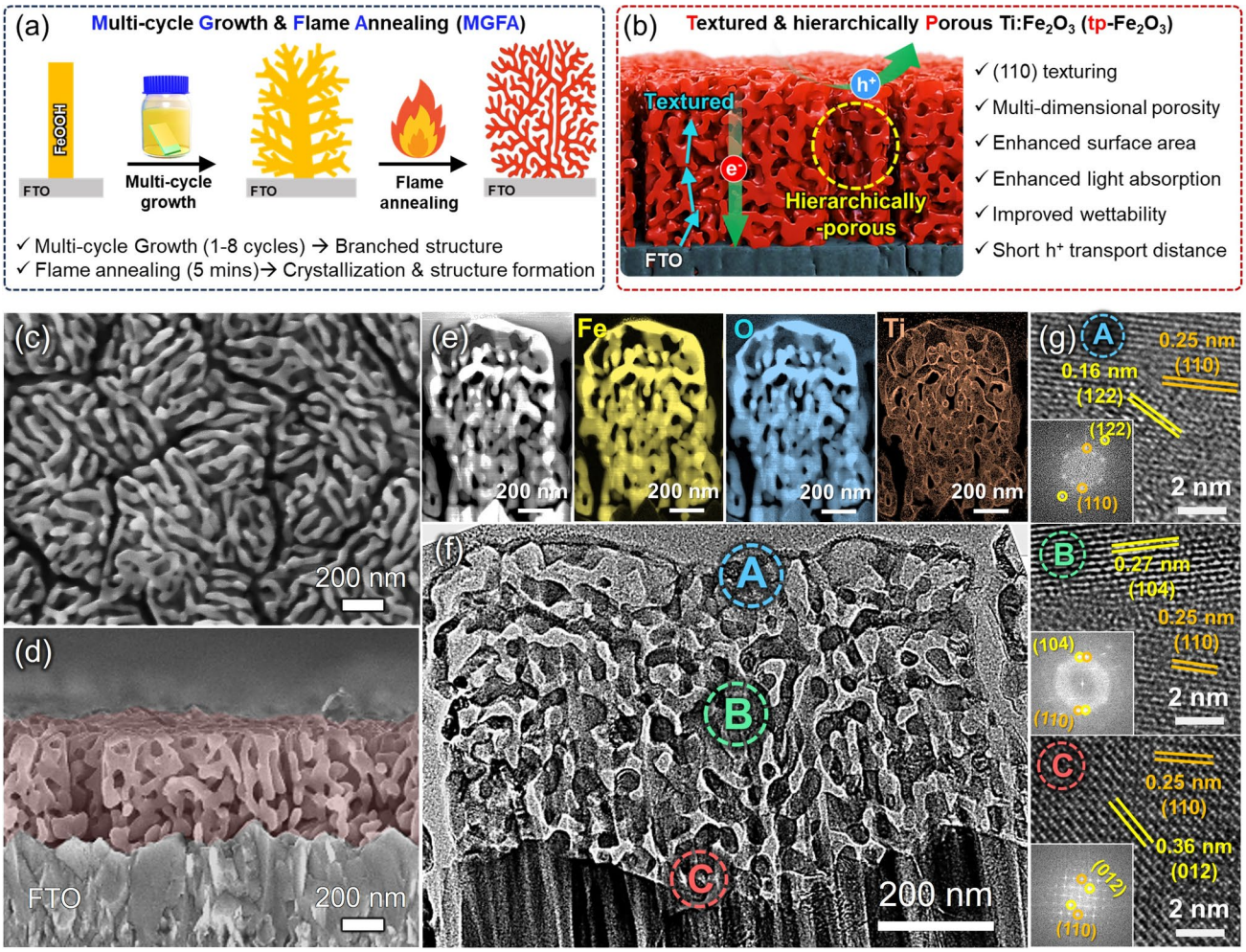

Fig. 1 Synthesis and structural features of tp-Fe_2O_3 via a MGFA method. **a** Schematic of the MGFA process. **b** Conceptual illustration of tp-Fe_2O_3 photoanode and its unique properties. **c, d** Top and cross-sectional SEM images of the synthesized tp-Fe_2O_3 photoanode. **e** TEM elemental mapping images via energy-dispersive spectroscopy (EDS) analysis. **f** Cross-sectional and **g** high-resolution TEM images with corresponding Fast Fourier Transform (FFT) patterns

further validating the well-crystallized structure. Notably, lattice fringes with a spacing of 0.25 nm, corresponding to the (110) planes, are consistently observed in vertical orientation in all three regions, indicating a preferential (110) orientation (i.e., texture) across different regions of the tp-Fe_2O_3 film [44, 45].

3.2 Crystal Structure, Composition, Optical, and Wettability Analysis

tp-Fe_2O_3 exhibits a distinct morphology from the typical nr-Fe_2O_3 (Fig. 2a), and we systematically compared their physicochemical properties. First, XRD analysis revealed that both tp-Fe_2O_3 and nr-Fe_2O_3 are consistent with the standard α-Fe_2O_3 phase (JCPDS #33–0664) and both exhibit a stronger (110) diffraction peak, indicating their preferential (110) orientation (Fig. 2b). The texture coefficient (TC) analysis (Fig. 2c) shows that both Fe_2O_3 display elevated TC values for the (110) plane compared to other planes. This is attributed to lattice matching between FeOOH and the underlying FTO substrate [46–49], as the substrate directs the crystallographic alignment during the growth. This substrate effect is further supported by a control sample deposited on quartz (Fig. S14). Although a comparable porous structure was formed under the same flame annealing

conditions, no (110) texture enhancement was observed. Furthermore, the TC value for tp-Fe_2O_3 is much higher than that of nr-Fe_2O_3, indicating that the multi-cycle growth process further promotes (110) texturing. This is evidenced by the enhanced (110) diffraction peak intensity and the progressive increase in TC with the increasing growth cycles in tp-Fe_2O_3 (Fig. S15). The progressive enhancement of (110) texturing with successive growth cycles is likely driven by the inherently lower surface energy of the (110) plane and its superior lattice compatibility with the FTO substrate, both of which render this orientation thermodynamically favorable and increasingly reinforced during repeated deposition [50, 51]. Based on previous literature, the (110) oriented facet in Fe_2O_3 is beneficial for the electron transport, facilitating charge separation and surface redox reactions [44].

To gain compositional insights across the depth of the Fe_2O_3 photoanodes, XPS depth profile analysis was performed on both tp-Fe_2O_3 and nr-Fe_2O_3 with a comparable film thickness of 550 nm (Figs. 2d, S16 and S17). For the nr-Fe_2O_3, the Ti dopant concentration gradually decreased from the surface to the bottom (gradient Ti doping). Conversely, the Sn content progressively increased toward the bottom, which was attributed to unintentional Sn diffusion from the underlying FTO substrate. Although Sn diffusion from the FTO substrate can increase carrier density, excessive incorporation may introduce trap sites, leading to recombination and impaired charge transport. In contrast, the tp-Fe_2O_3 displayed a uniform Ti doping profile throughout the film and a significantly lower Sn concentration at the bottom. Uniform Ti distribution in the Fe_2O_3 ensures consistent bulk conductivity and a stable internal electric field, promoting charge separation and reducing recombination. Consequently, charge transport to the photoanode surface is enhanced.

Figure 2e illustrates the lateral grain size distribution of tp-Fe_2O_3 and nr-Fe_2O_3 photoanodes (obtained from SEM and TEM images), providing insight into the microstructural characteristics of the synthesized Fe_2O_3. The average lateral grain size of tp-Fe_2O_3 is determined to be approximately 27.1 ± 5.7 nm, while the average size for nr-Fe_2O_3 is two times larger, around 51.3 ± 6.9 nm. The lateral grain size distribution affects the electronic properties of the photoanodes; The reduced grain size in tp-Fe_2O_3 leads to a higher density of grain boundaries and enlarged surface area, which facilitates the formation of multiple surface-confined electric fields that enhance charge separation and suppress recombination [43]. Moreover, the reduced lateral grain size minimizes the carrier transport distance to the surface, which is particularly beneficial for Fe_2O_3 due to its intrinsically short hole diffusion length (2–4 nm) [20, 25, 43]. In addition, Raman analysis (Fig. S18) reveals that tp-Fe_2O_3 has a smaller normalized E_u peak intensity (I_{Eu}/I_{A1g}), indicating its enhanced structural order, better-preserved lattice symmetry, and lower strain [52–54]. Overall, the structure of tp-Fe_2O_3 ensures that photogenerated carriers are efficiently transported to the reactive surface, improving the overall PEC performance.

We analyzed the pore size distribution and specific surface area of tp-Fe_2O_3 and nr-Fe_2O_3 by the BET method (Fig. S19). As shown in Fig. 2f, tp-Fe_2O_3 exhibits a hierarchically porous structure with mesopores and nanopores (< 10 nm), whereas nr-Fe_2O_3 contains few nanopores and negligible mesoporosity. Correspondingly, the tp-Fe_2O_3 possesses nearly twice the specific surface area and over ten times the total pore volume relative to nr-Fe_2O_3 (Fig. 2g). On the other hand, as shown in Fig. 2h, tp-Fe_2O_3 exhibits a significantly lower contact angle (11°) than nr-Fe_2O_3 (31°), indicating high surface wettability. This improved wettability is attributed to the hierarchically porous structure, which facilitates capillary-driven electrolyte infiltration and increases the effective contact area [55, 56]. The higher work of adhesion observed for tp-Fe_2O_3 further confirms its enhanced surface affinity with the electrolyte, thereby promoting more efficient interfacial charge transfer during PEC reactions. Finally, the optical properties of tp-Fe_2O_3 and nr-Fe_2O_3 photoanodes with similar film thickness (~ 550 nm) were analyzed (Fig. 2i). UV–Vis absorbance measurements reveal that tp-Fe_2O_3 exhibits noticeably higher absorbance across the 300–600 nm range compared to nr-Fe_2O_3. This enhancement is attributed to its hierarchically porous morphology, which promotes light scattering and internal reflection, thereby extending the optical path length and improving photon capture efficiency [57, 58].

In summary, the tp-Fe_2O_3 photoanode prepared by the MGFA method, compared to typical nr-Fe_2O_3, has a hierarchically porous architecture, a higher degree of (110) texture, homogeneous dopant distribution, and an enlarged surface area, as well as superior wettability (Fig. S20). These integrated properties are expected to enhance light absorption, facilitate reactant diffusion, and provide abundant active sites, which are highly beneficial for PEC reactions.

 https://doi.org/10.1007/s40820-025-02045-z

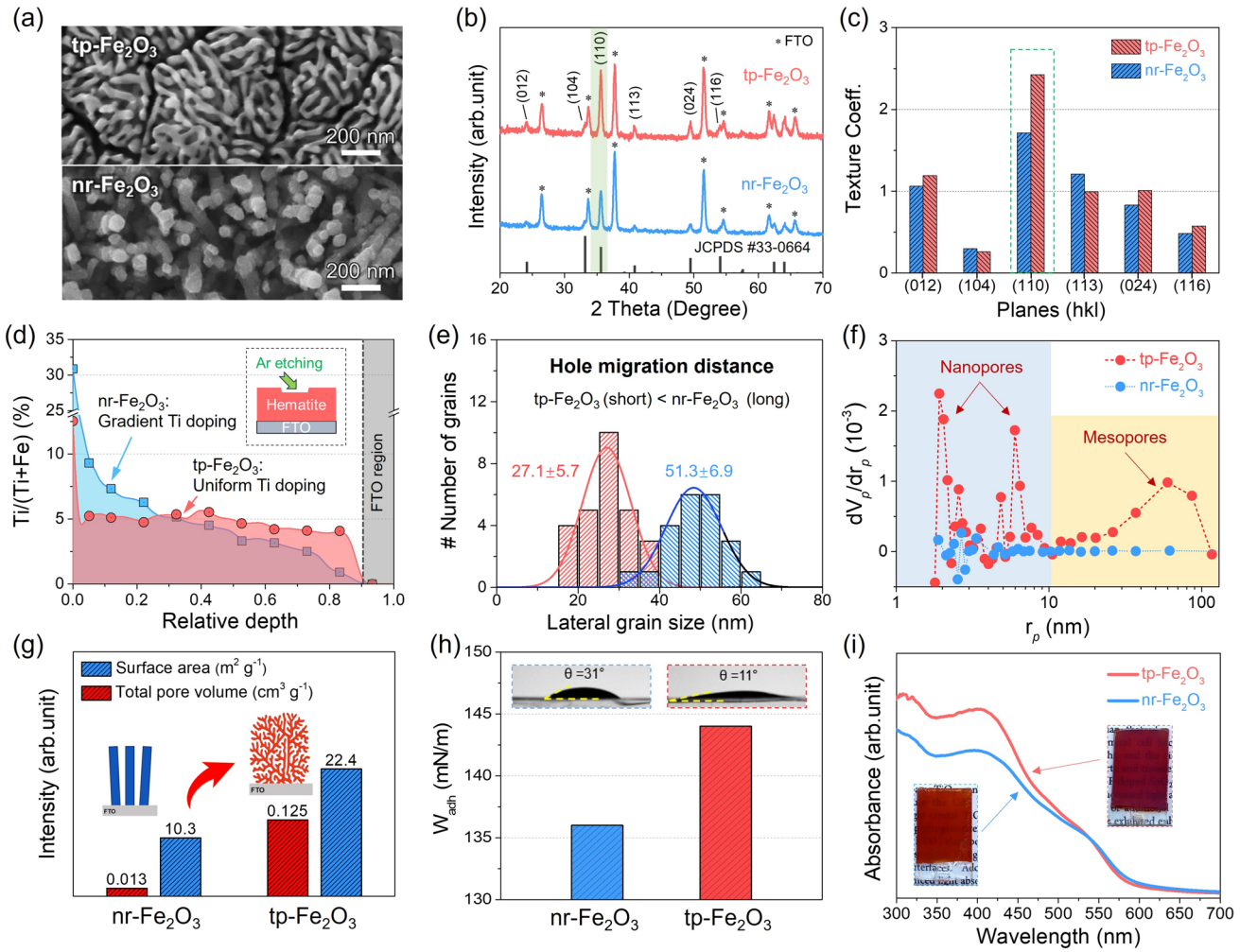

Fig. 2 Comparative physicochemical properties of tp-Fe_2O_3 and nr-Fe_2O_3 photoanodes. **a** Top-view SEM images. **b** XRD pattern and **c** TC analysis. **d** Ti dopant depth profile. **e** Lateral grain size distribution. **f** BJH pore size distribution. **g** Comparison of BET surface area and total pore volume. **h** Contact angle and work of adhesion analyses. **i** UV–Vis absorbance spectra. The inset shows photographs of tp-Fe_2O_3 and nr-Fe_2O_3 photoanodes

3.3 Bulk and Interfacial Charge Carrier Dynamics Analysis

We further investigated the impact of structural and compositional differences between tp-Fe_2O_3 and nr-Fe_2O_3 photoanodes on both bulk and interfacial properties through a series of charge dynamics measurements. First, the electrochemically active surface area (ECSA), which reflects the number of accessible surface sites for interfacial charge transfer (Fig. 3a) [59, 60], was assessed by recording the capacitive current density at various scan rates (Fig. S21). The slope of the tp-Fe_2O_3 curve is 2.1 times that of the nr-Fe_2O_3; accordingly, its ECSA value is 2.1 times higher, caused by its hierarchically porous structure. Second, the donor density (N_D) and depletion layer width (W_D) for tp-Fe_2O_3 and nr-Fe_2O_3 were determined from the Mott–Schottky plots (Fig. S22). tp-Fe_2O_3 exhibits about twenty-four times higher donor density (3.1×10^{21} cm^{-3}) than nr-Fe_2O_3 (1.3×10^{20} cm^{-3}), along with a five times smaller depletion width of approximately 1.3 nm, compared to 6.4 nm for nr-Fe_2O_3 (Fig. 3b). A higher donor density indicates that tp-Fe_2O_3 is more conductive due to its more uniform Ti doping distribution. A smaller depletion layer width in tp-Fe_2O_3 indicates enhanced charge accumulation near the interface, which not only minimizes bulk recombination losses but also improves charge extraction efficiency at the interface

[61]. These features directly address the intrinsically short hole diffusion length of hematite [62].

We further performed electrochemical impedance spectroscopy (EIS) for both tp-Fe_2O_3 and nr-Fe_2O_3 photoanodes under illumination to evaluate the charge recombination process. The EIS-derived Bode plots (Fig. 3c) show that the phase peak maxima (F_{max}) for tp-Fe_2O_3 and nr-Fe_2O_3 occur at 20.4 and 51.4 Hz, and the corresponding electron lifetimes (τ_n) calculated by the equation, $\tau_n = 1/(2\pi F_{max})$, are 7.8 and 3.1 ms, respectively. This result suggests that tp-Fe_2O_3 has slower interfacial recombination and more efficient separation compared to those of nr-Fe_2O_3. In addition, potentiostatic electrochemical impedance spectroscopy (PEIS) measurements in Figs. S23 and S24 show that tp-Fe_2O_3 exhibits consistently lower bulk charge transport (R_{bulk}) and interfacial charge transfer resistance (R_{ct}), and higher C_{bulk} and C_{trap}, suggesting greater charge accumulation in both the space charge region and surface states [63]. The charge transfer rate constant ($K_{transfer}$), calculated as $K_{transfer} = 1/(R_{ct} \times C_{trap})$, is higher for tp-$Fe_2O_3$ across the entire potential range, confirming its superior charge transfer kinetics at the hematite/electrolyte interface (Fig. 3d). This is further supported by its much slower transient photocurrent decay and superior charge retention compared to nr-Fe_2O_3 (Fig. S25).

Figure 3e shows Kelvin probe force microscopy (KPFM) maps of the surface potential for tp-Fe_2O_3 and nr-Fe_2O_3 in the dark (left) and under illumination (right) [64]. In these maps, warmer colors (red/yellow) indicate higher surface potential. A shift to warmer colors upon illumination reflects light-induced charge separation and the accumulation of photogenerated carriers at the surface. Compared to the nr-Fe_2O_3, the tp-Fe_2O_3 photoanode exhibits a more substantial color shift and a larger potential change between light and dark ($V_{light} - V_{dark} = 89$ mV; Figs. 3f and S26), indicating more efficient surface charge separation and accumulation at the electrode surface.

Finally, the charge transport ($\eta_{transport}$) and charge transfer efficiencies ($\eta_{transfer}$) were calculated using the hole scavenger method (Figs. 3g, h, and S27) [65]. Across the entire potential range, the tp-Fe_2O_3 photoanode exhibits consistently higher $\eta_{transport}$ and $\eta_{transfer}$ than those of nr-Fe_2O_3. The larger $\eta_{transport}$ for tp-Fe_2O_3 comes from the suppressed bulk recombination and improved carrier mobility in tp-Fe_2O_3, attributed to its pronounced (110) texturing (Figs. 2c and S15) and uniform dopant distribution (Figs. 1e and S16) [48]. The larger $\eta_{transfer}$ stems from more efficient utilization of interfacial holes, enabled by its hierarchically porous architecture and thin lateral grain size (Fig. 2e), which promotes effective charge separation and accelerates surface reaction kinetics (Fig. 3d-f) [43]. Notably, while high transfer efficiencies (over 80%) are occasionally reported, simultaneously achieving a high transport efficiency exceeding 30% is particularly significant for hematite photoanodes, distinguishing tp-Fe_2O_3 from many commonly utilized 1D nanorod structures and even multi-elements-doped systems.

Activation energies (E_a) for the OER were determined by analyzing the Arrhenius plot of temperature-dependent J–V data. J–V curves measured at various temperatures (Fig. S28) were used to construct ln(J) versus 1/T plots (Fig. 3i), and E_a values were extracted from the slopes of the linear fit [66]. The tp-Fe_2O_3 exhibits much lower E_a (9.9 meV) than nr-Fe_2O_3 (27.4 meV), indicating faster kinetics, enhanced charge transfer dynamics, and a reduced energy barrier for water oxidation, consistent with the above charge dynamic analysis results.

3.4 Photoelectrochemical (PEC) Performance

We next investigate how the structural advantages and enhanced charge dynamics of tp-Fe_2O_3 affect its PEC performance compared to nr-Fe_2O_3 (Fig. 4). Under 1 Sun illumination, tp-Fe_2O_3 achieves an OER photocurrent density of 3.1 mA cm^{-2} at 1.23 V_{RHE} (Fig. 4a), more than twice that of nr-Fe_2O_3 (1.4 mA cm^{-2}). In addition, tp-Fe_2O_3 exhibits a higher incident photon-to-current efficiency (IPCE), reaching a peak value of 52% at 390 nm (Fig. S29), along with improved applied bias photon-to-current efficiency (ABPE) and absorbed photon-to-current efficiency (APCE) compared to nr-Fe_2O_3 (Fig. S30). As shown in Fig. 4b, tp-Fe_2O_3 also exhibits excellent stability, retaining 97% of its initial photocurrent density after 105 h with no apparent morphological change (SEM insets). In contrast, nr-Fe_2O_3 retains only 72% after 20 h. In addition, the gas evolution of tp-Fe_2O_3 during PEC water splitting was quantified using gas chromatography, and the average Faradaic efficiencies (FE) for H_2 and O_2 production were calculated to be approximately 80% (Fig. S31).

Next, we investigated the potential to replace the sluggish OER with the kinetically more favorable HzOR by utilizing tp-Fe_2O_3 to enhance H_2 production [67]. HzOR is appealing because N_2H_4 is a widely used chemical compound

 https://doi.org/10.1007/s40820-025-02045-z

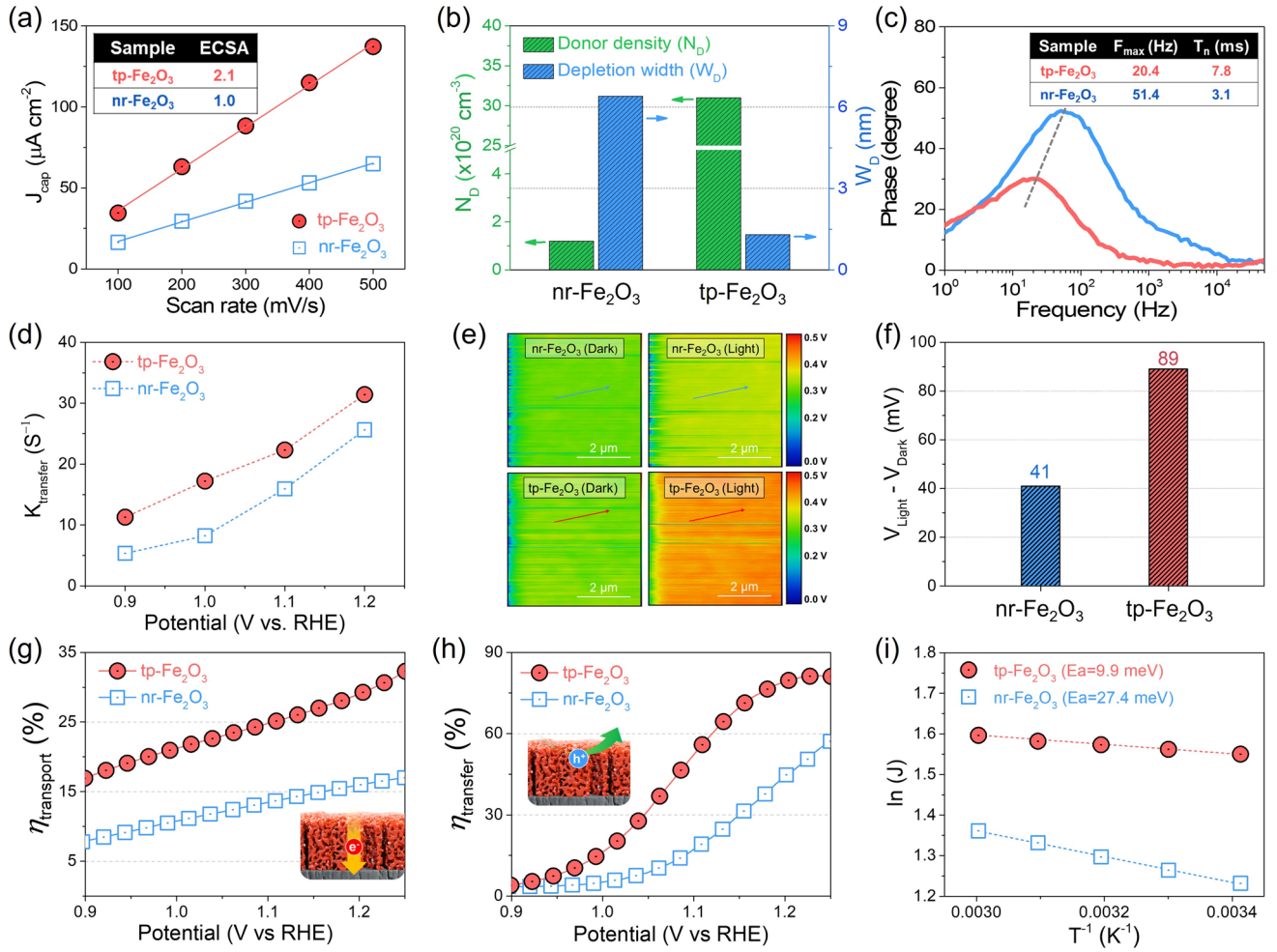

Fig. 3 Bulk and interfacial charge carrier dynamics of tp-Fe_2O_3 and nr-Fe_2O_3 photoanodes. **a** Electrochemical active surface area (ECSA) comparison. **b** Donor density (N_D) and depletion layer width (W_D) derived from the Mott–Schottky measurement. **c** Bode phase plot. **d** Surface charge transfer rate constant ($K_{transfer} = 1/(R_{ct} \times C_{trap})$, R_{ct} represents the resistance between the photoanode and the electrolyte, and C_{trap} is the capacitance associated with charge accumulation on the surface states. **e** Surface potential distribution and **f** illumination-induced shift (ΔV) from Kelvin probe force microscopy (KPFM). **g** Charge transport and **h** transfer efficiencies. **i** Arrhenius plots of ln(J) vs. 1/T at 1.6 V_{RHE} and corresponding activation energies

(Fig. S32) across diverse industries. However, it is highly toxic to health and the environment (Table S1). PEC HzOR coupled with HER provides a strategy for simultaneously remediating N_2H_4 to benign N_2 and boosting H_2 production (Fig. 4c and Table S2) [68]. HzOR, compared to the OER, proceeds at a substantially lower theoretical potential (-0.33 V_{RHE}) and exhibits superior reaction kinetics [69]. Density functional theory (DFT) free energy profile reveals that the potential-determining step (PDS) for OER on Ti-doped Fe_2O_3 (110) is *OH to *O with an energy barrier 1.26 eV, whereas for the HzOR, the $*N_2H_4$ to $*N_2H_3$ PDS step exhibits a much lower energy barrier of 0.33 eV. This value is even smaller than that of the PDS for H_2O_2 oxidation (0.48 eV), indicating much more favorable thermodynamics for HzOR (Figs. S33 and S34).

Figure 4d shows that the photocurrent density of the tp-Fe_2O_3 photoanode is increased from 3.1 mA cm^{-2} for OER to 7.1 mA cm^{-2} for HzOR at 1.23 V_{RHE}. The onset potential is greatly shifted cathodically to 0.6 V_{RHE}. Notably, the tp-Fe_2O_3 photoanode with HzOR achieves a photocurrent density of approximately 10 mA cm^{-2} at a higher potential of 1.6 V_{RHE}, corresponding to nearly 80% of Fe_2O_3's theoretical maximum photocurrent density. Similar benefits of using HzOR over OER were also observed for the nr-Fe_2O_3 photoanode (Fig. S35). The tp-Fe_2O_3 photoanode also exhibits good stability, with negligible degradation over 10 h

of continuous operation under HzOR (Fig. 4e). During the stability test, we observed vigorous H_2 bubble formation on the Pt mesh counter electrode with HzOR, in contrast to the OER condition, and the H_2 production rate under HzOR is 2.2 times higher than that driven by OER (Fig. S36). The measured FE were 80.4% for H_2, 62.8% for N_2, and 19.1% for O_2 (Figs. 4f and S37), and the combined amount of anodic gas (N_2 and O_2) was approximately half that of the evolved H_2, consistent with the expected stoichiometry.

Figure 4g compares the photocurrent densities at 1.23 V_{RHE} for Fe_2O_3 photoanodes without oxygen evolution co-catalysts (OEC) under both OER and AOR conditions. In both cases, our tp-Fe_2O_3 photoanode surpasses most of the previously reported values for bare Fe_2O_3 systems. To the best of our knowledge, our tp-Fe_2O_3 achieves a high photocurrent density of 7.1 mA cm^{-2} at 1.23 V_{RHE} under HzOR conditions, which exceeds all previously reported values for Fe_2O_3-based photoanodes, under both water oxidation and alternative anodic reaction pathways (Tables S3 and S4).

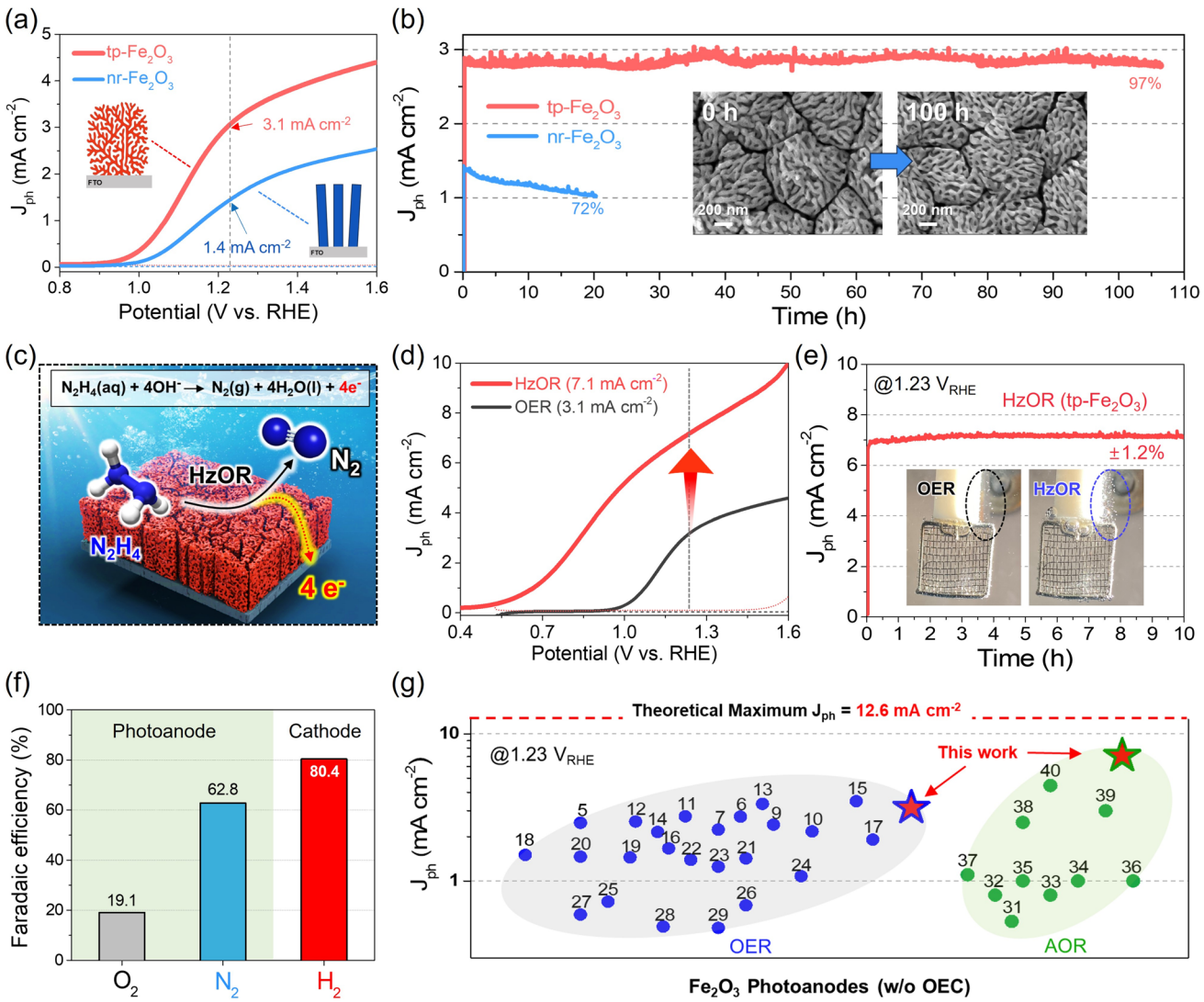

Fig. 4 Photoelectrochemical (PEC) oxygen evolution reaction (OER) and hydrazine oxidation reaction (HzOR) performance of Fe_2O_3 photoanodes. **a** Photocurrent density-potential (J–V) and **b** photocurrent stability curves of nr- and tp-Fe_2O_3 photoanodes in 1 M NaOH (pH 13.6). Inset: SEM morphology change after 100 h of operation. **c** Schematic of PEC HzOR system. HzOR in alkaline electrolyte generates N_2, H_2O, and four electrons. **d** J–V and **e** chronoamperometry curves of tp-Fe_2O_3 for PEC HzOR. Inset: photographs of H_2 bubble generation at the Pt cathode. **f** Faradaic efficiency (FE) for O_2, N_2, and H_2. **g** Literature comparison of Fe_2O_3-based photoanodes (without OEC) for OER and various alternative oxidation reactions (AOR), the corresponding reference numbers are taken from Tables S3 and S4

https://doi.org/10.1007/s40820-025-02045-z

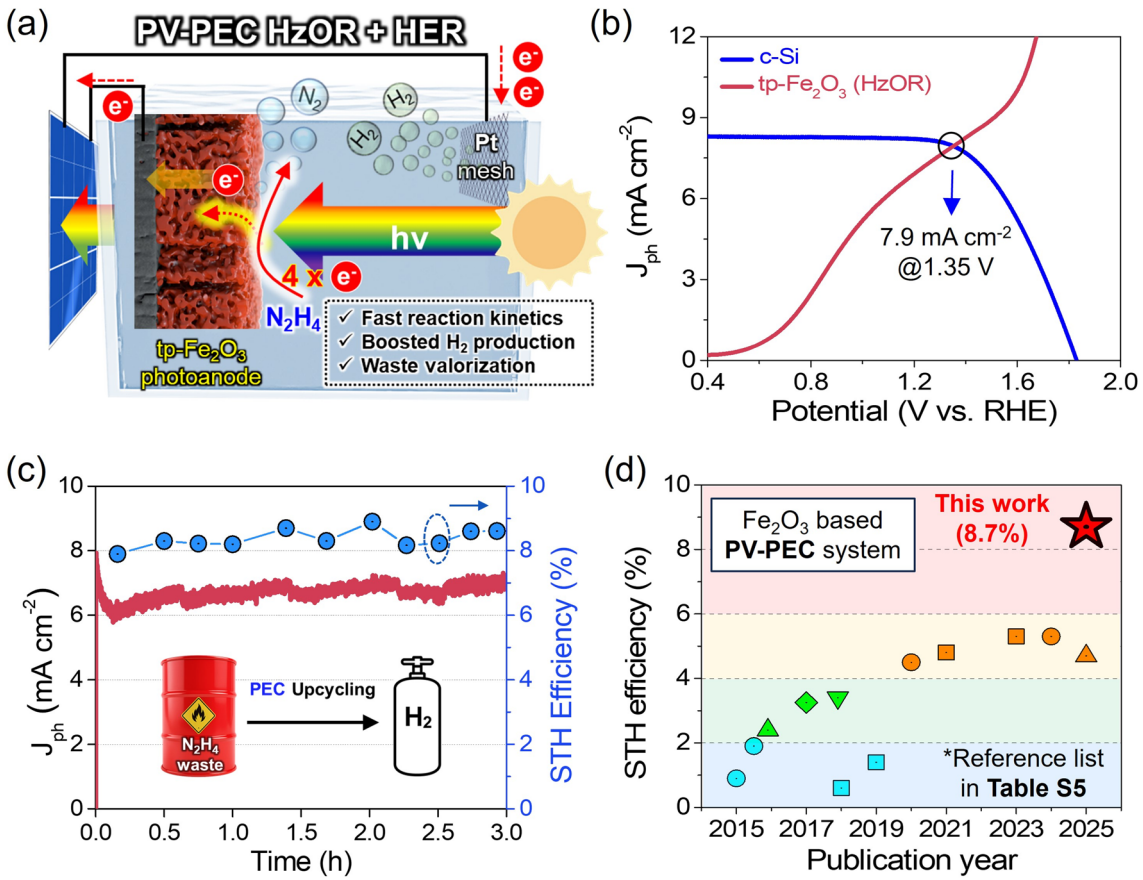

Fig. 5 Integrated PV-PEC system for hydrazine-boostered hydrogen production without external bias. **a** Schematic illustration of the integrated PV-PEC tandem system. **b** J–V curves of the c-Si solar cell (behind tp-Fe_2O_3 photoanode) and PEC HzOR cell under simulated sunlight illumination (1 sun, 100 mW cm^{-2}). The intersection indicates the operating point for unbiased water splitting. **c** Chronoamperometric stability under bias-free PEC HzOR. **d** Comparison of the solar-to-hydrogen (STH) efficiencies reported for Fe_2O_3-based PV-PEC tandem systems

3.5 Solar-Powered Hydrazine Oxidation Reaction Coupled with H_2 Production

We finally demonstrated the practical applicability of the tp-Fe_2O_3 photoanode for solar-powered H_2 production by integrating a commercial Si solar cell with the tp-Fe_2O_3 photoelectrode under HzOR conditions (Figs. 5a and S38). The J–V curves of the Si solar cell (stack behind tp-Fe_2O_3) and the tp-Fe_2O_3 photoanode under HzOR conditions intersect at 1.35 V and 7.9 mA cm^{-2} (Fig. 5b), confirming the feasibility of spontaneous H_2 production without external bias. The integrated PV-PEC system enables hydrazine-boosted H_2 production under continuous solar illumination for 3 h (Fig. 5c), reaching a maximum STH efficiency of 8.7%. To the best of our knowledge, this represents the highest reported STH efficiency for Fe_2O_3-based PV-PEC systems (Fig. 5d and Table S5).

4 Conclusion

We addressed intrinsic limitations of hematite as a PEC photoanode, including a short hole diffusion length, low conductivity, and sluggish OER kinetics, through a synergistic co-design of the Fe_2O_3 photoanode architecture and surface reaction pathway. We developed a new multi-cycle growth and flame annealing method to synthesize a tp-Fe_2O_3 photoanode, featuring a strong (110) texture, uniform Ti distribution, an enlarged surface area, hierarchically porosity, and a thinner lateral grain size. In comparison to typical nr-Fe_2O_3, this architecture delivers markedly improved bulk charge transport and interfacial charge transfer, yielding an OER photocurrent of 3.1 mA cm^{-2} at 1.23 V_{RHE} without any co-catalyst and exceptional stability over 105 h. When we further replace the sluggish OER with the HzOR, a photocurrent density of 7.1 mA cm^{-2} is achieved at 1.23 V_{RHE},

the highest value reported for Fe_2O_3-based photoanodes to date. Furthermore, integration of tp-Fe_2O_3 into a bias-free PV-PEC tandem system with a commercial Si solar cell yields a solar-to-hydrogen efficiency of 8.7%, representing the highest reported value for Fe_2O_3-based PV-tandem devices. These results provide clear design guidelines for Fe_2O_3 photoanodes and highlight HzOR as a sustainable, highly efficient alternative pathway for solar fuel production.

Acknowledgements This work was supported by a National Research Foundation of Korea (NRF) grant funded by the Korean government (MSIT) (No.RS-2024-00335976). The authors acknowledge the Korea Institute of Science and Technology Information (KISTI) for providing computational resources through the Nurion supercomputing system. The authors are also grateful to Ji Kwon Bae from Seoul National University for providing support with the KPFM measurements.

Author Contributions Runfa Tan: Conceptualization, investigation, methodology, formal analysis, validation, writing—original draft, writing—review and editing, data curation. Yoo Jae Jeong: Investigation, formal analysis, writing—review and editing. Hyun Soo Han: Investigation, formal analysis, methodology, data curation, supervision. Samadhan Kapse: Formal analysis, software. Seong Sik Shin: Supervision. Xiaolin Zheng: Writing—review and editing, project administration, supervision. In Sun Cho: Conceptualization, writing—review and editing, funding acquisition, project administration, supervision.

Declarations

Conflict of Interests The authors declare no conflict of interest. They have no known competing financial interests or personal relationships that could have influenced the work reported in this paper.

Supplementary Information The online version contains supplementary material available at https://doi.org/10.1007/s40820-025-02045-z.

References

1. K. He, Z. Huang, C. Chen, C. Qiu, Y.L. Zhong et al., Exploring the roles of single atom in hydrogen peroxide photosynthesis. Nano-Micro Lett. **16**, 23 (2024). https://doi.org/10.1007/s40820-023-01231-1
2. M. Abbas, S. Chen, Z. Li, M. Ishaq, Z. Zheng et al., Highest solar-to-hydrogen conversion efficiency in Cu_2ZnSnS_4 photocathodes and its directly unbiased solar seawater splitting. Nano-Micro Lett. **17**, 257 (2025). https://doi.org/10.1007/s40820-025-01755-8
3. Y. Guo, X. Tong, N. Yang, Photocatalytic and electrocatalytic generation of hydrogen peroxide: principles, catalyst design and performance. Nano-Micro Lett. **15**, 77 (2023). https://doi.org/10.1007/s40820-023-01052-2
4. C. Jiang, S.J.A. Moniz, A. Wang, T. Zhang, J. Tang, Photoelectrochemical devices for solar water splitting–materials and challenges. Chem. Soc. Rev. **46**(15), 4645–4660 (2017). https://doi.org/10.1039/c6cs00306k
5. B. He, Y. Cao, K. Lin, Y. Wang, Z. Li et al., Strong interactions between Au nanoparticles and $BiVO_4$ photoanode boosts hole extraction for photoelectrochemical water splitting. Angew. Chem. Int. Ed. **63**(23), e202402435 (2024). https://doi.org/10.1002/anie.202402435
6. K.-J. Lin, B. He, Z.-H. Xiao, L.-Y. Li, Z.-Y. Qiao et al., Electron-rich Mn: NiFe-LDHs onto BiVO4 photoanode for improved photoelectrochemical water splitting. Rare Met. **44**(10), 7476–7485 (2025). https://doi.org/10.1007/s12598-025-03494-6
7. Y. Cao, Y. Tian, B. He, Z. Qiao, L. Li et al., Modulating hole extraction and water oxidation kinetics in CoPi/Au/$BiVO_4$ photoanode *via* strong metal-support interactions. J. Energy Chem. **109**, 315–324 (2025). https://doi.org/10.1016/j.jechem.2025.05.048
8. G. Gao, Z. Sun, X. Chen, Z. Guang, B. Sun et al., Recent advances in hydrogen production coupled with alternative oxidation reactions. Coord. Chem. Rev. **509**, 215777 (2024). https://doi.org/10.1016/j.ccr.2024.215777
9. Y. Miao, M. Shao, Photoelectrocatalysis for high-value-added chemicals production. Chin. J. Catal. **43**(3), 595–610 (2022). https://doi.org/10.1016/S1872-2067(21)63923-2
10. R.-Y. Fan, X.-J. Zhai, W.-Z. Qiao, Y.-S. Zhang, N. Yu et al., Optimized electronic modification of S-doped CuO induced by oxidative reconstruction for coupling glycerol electrooxidation with hydrogen evolution. Nano-Micro Lett. **15**, 190 (2023). https://doi.org/10.1007/s40820-023-01159-6
11. S. Li, D. Liu, G. Wang, P. Ma, X. Wang et al., Vertical 3D nanostructures boost efficient hydrogen production coupled with glycerol oxidation under alkaline conditions. Nano-Micro Lett. **15**, 189 (2023). https://doi.org/10.1007/s40820-023-01150-1
12. S. Hong, J. Kim, J. Park, S. Im, M.R. Hoffmann et al., Scalable Ir-doped $NiFe_2O_4/TiO_2$ heterojunction anode for decentralized saline wastewater treatment and H_2 production. Nano-Micro Lett. **17**, 51 (2025). https://doi.org/10.1007/s40820-024-01542-x

13. C. Yang, H. Pang, X. Li, X. Zheng, T. Wei et al., Scalable electrocatalytic urea wastewater treatment coupled with hydrogen production by regulating adsorption behavior of urea molecule. Nano-Micro Lett. **17**(1), 159 (2025). https://doi.org/10.1007/s40820-024-01585-0
14. X. Gao, Y. Chen, Y. Wang, L. Zhao, X. Zhao et al., Next-generation green hydrogen: progress and perspective from electricity, catalyst to electrolyte in electrocatalytic water splitting. Nano-Micro Lett. **16**, 237 (2024). https://doi.org/10.1007/s40820-024-01424-2
15. Z. Chen, R. Zheng, T. Bao, T. Ma, W. Wei et al., Dual-doped nickel sulfide for electro-upgrading polyethylene terephthalate into valuable chemicals and hydrogen fuel. Nano-Micro Lett. **15**, 210 (2023). https://doi.org/10.1007/s40820-023-01181-8
16. S. Shen, Y. Li, L. Ouyang, L. Zhang, M. Zhu et al., V-Ti-based solid solution alloys for solid-state hydrogen storage. Nano-Micro Lett. **17**, 175 (2025). https://doi.org/10.1007/s40820-025-01672-w
17. M. Wang, X. Wang, E. Sun, Z. Kang, F. Gong et al., Advancements and innovations in low-temperature hydrogen electrochemical conversion devices driven by 3D printing technology. Nano-Micro Lett. **18**(1), 61 (2025). https://doi.org/10.1007/s40820-025-01907-w
18. J. Li, N. Wu, J. Zhang, H.-H. Wu, K. Pan et al., Machine learning-assisted low-dimensional electrocatalysts design for hydrogen evolution reaction. Nano-Micro Lett. **15**(1), 227 (2023). https://doi.org/10.1007/s40820-023-01192-5
19. F. Wang, L. Xie, N. Sun, T. Zhi, M. Zhang et al., Deformable catalytic material derived from mechanical flexibility for hydrogen evolution reaction. Nano-Micro Lett. **16**(1), 32 (2023). https://doi.org/10.1007/s40820-023-01251-x
20. B.K. Jha, S. Chaule, J.-H. Jang, Enhancing photocatalytic efficiency with hematite photoanodes: principles, properties, and strategies for surface, bulk, and interface charge transfer improvement. Mater. Chem. Front. **8**(10), 2197–2226 (2024). https://doi.org/10.1039/D3QM01100C
21. D. Zhou, K. Fan, Recent strategies to enhance the efficiency of hematite photoanodes in photoelectrochemical water splitting. Chin. J. Catal. **42**(6), 904–919 (2021). https://doi.org/10.1016/S1872-2067(20)63712-3
22. J. Kang, B.G. Ghule, S.G. Gyeong, S.-J. Ha, J.-H. Jang, Alleviating charge recombination caused by unfavorable interaction of P and Sn in hematite for photoelectrochemical water oxidation. ACS Catal. **14**(13), 10355–10364 (2024). https://doi.org/10.1021/acscatal.4c01150
23. H. Niu, L. Gao, M. Liu, Y. Zou, J. Wang et al., Rapid charge extraction *via* hole transfer layer and interfacial coordination bonds on hematite photoanode for efficient photoelectrochemical water oxidation. Appl. Catal. B Environ. Energy **358**, 124369 (2024). https://doi.org/10.1016/j.apcatb.2024.124369
24. J. Park, K.-Y. Yoon, B.G. Ghule, H. Kim, J.-H. Jang, Morphology-engineered hematite photoanode for photoelectrochemical water splitting. ACS Energy Lett. **9**(6), 3169–3176 (2024). https://doi.org/10.1021/acsenergylett.4c01347
25. K. Kang, C. Tang, J.H. Kim, W.J. Byun, J.H. Lee et al., *In situ* construction of ta: Fe_2O_3@$CaFe_2O_4$ Core-Shell nanorod p–t–n heterojunction photoanodes for efficient and robust solar water oxidation. ACS Catal. **13**(10), 7002–7012 (2023). https://doi.org/10.1021/acscatal.3c00932
26. H. Wang, C. Xu, M. Ye, K. Liang, Y. Zhang et al., Inducing multiporous hematite nanorod photoanode by zirconium oxide overlayer and niobium oxide underlayer for efficient solar water splitting. Small **21**(23), 2502503 (2025). https://doi.org/10.1002/smll.202502503
27. C. Xu, H. Wang, H. Guo, K. Liang, Y. Zhang et al., Parallel multi-stacked photoanodes of Sb-doped p-n homojunction hematite with near-theoretical solar conversion efficiency. Nat. Commun. **15**(1), 9712 (2024). https://doi.org/10.1038/s41467-024-53967-y
28. L. He, Q. Zhang, C. Gong, H. Liu, F. Hu et al., The dual-function of hematite-based photoelectrochemical sensor for solar-to-electricity conversion and self-powered glucose detection. Sens. Actuat. B Chem. **310**, 127842 (2020). https://doi.org/10.1016/j.snb.2020.127842
29. J. Yuan, Y. Yuan, J. Zhang, H. Xu, Z. Mao et al., Mechanistic insights into selective acetaldehyde formation from ethanol oxidation on hematite photoanodes by operando spectroelectrochemistry. Chemsuschem **15**(5), e202102313 (2022). https://doi.org/10.1002/cssc.202102313
30. X. Li, J. Wang, M. Sun, X. Qian, Y. Zhao, Ti–Fe_2O_3/Ni(OH) as an efficient and durable photoanode for the photoelectrochemical catalysis of PET plastic to formic acid. J. Energy Chem. **78**, 487–496 (2023). https://doi.org/10.1016/j.jechem.2022.12.031
31. C.A. Mesa, A. Kafizas, L. Francàs, S.R. Pendlebury, E. Pastor et al., Kinetics of photoelectrochemical oxidation of methanol on hematite photoanodes. J. Am. Chem. Soc. **139**(33), 11537–11543 (2017). https://doi.org/10.1021/jacs.7b05184
32. L. Zhu, Z. Li, Y. Cheng, X. Zhang, H. Du et al., A highly efficient hematite photoelectrochemical fuel cell for solar-driven hydrogen production. Int. J. Hydrog. Energy **48**(84), 32699–32707 (2023). https://doi.org/10.1016/j.ijhydene.2023.05.042
33. X. Sun, X. Jiang, Z. Wang, Y. Li, J. Ren et al., Fluorescent probe for imaging N_2H_4 in plants, food, and living cells and for quantitative detection of N_2H_4 in soil and water using a smartphone. J. Hazard. Mater. **479**, 135701 (2024). https://doi.org/10.1016/j.jhazmat.2024.135701
34. R. Tan, Y.J. Jeong, Q. Li, M. Kang, I.S. Cho, Defect-rich spinel ferrites with improved charge collection properties for efficient solar water splitting. J. Adv. Ceram. **12**(3), 612–624 (2023). https://doi.org/10.26599/jac.2023.9220709
35. Y.J. Jeong, R. Tan, S. Nam, J.H. Lee, S.K. Kim et al., Rapid surface reconstruction of In_2S_3 photoanode *via* flame treatment for enhanced photoelectrochemical performance. Adv. Mater. **37**(26), 2403164 (2025). https://doi.org/10.1002/adma.202403164
36. I.S. Cho, H.S. Han, M. Logar, J. Park, X. Zheng, Enhancing low-bias performance of hematite photoanodes for solar water splitting by simultaneous reduction of bulk, interface,

and surface recombination pathways. Adv. Energy Mater. **6**(4), 1501840 (2016). https://doi.org/10.1002/aenm.201501840

37. I.S. Cho, M. Logar, C.H. Lee, L. Cai, F.B. Prinz et al., Rapid and controllable flame reduction of TiO_2 nanowires for enhanced solar water-splitting. Nano Lett. **14**(1), 24–31 (2014). https://doi.org/10.1021/nl4026902
38. I.S. Cho, C.H. Lee, Y. Feng, M. Logar, P.M. Rao et al., Codoping titanium dioxide nanowires with tungsten and carbon for enhanced photoelectrochemical performance. Nat. Commun. **4**, 1723 (2013). https://doi.org/10.1038/ncomms2729
39. R. Tan, S.Y. Hong, Y.J. Jeong, S.S. Shin, I.S. Cho, Interfacial engineering and rapid thermal crystallization of Sb_2S_3 photoanodes for enhanced photoelectrochemical performances. J. Energy Chem. **108**, 417–426 (2025). https://doi.org/10.1016/j.jechem.2025.04.044
40. J. Zou, C.-Z. Li, C.-Y. Chang, H.-L. Yip, A.K.Y. Jen, Interfacial engineering of ultrathin metal film transparent electrode for flexible organic photovoltaic cells. Adv. Mater. **26**(22), 3618–3623 (2014). https://doi.org/10.1002/adma.201306212
41. T. Butburee, Y. Bai, H. Wang, H. Chen, Z. Wang et al., 2D porous TiO_2 single-crystalline nanostructure demonstrating high photo-electrochemical water splitting performance. Adv. Mater. **30**(21), 1705666 (2018). https://doi.org/10.1002/adma.201705666
42. R. Tan, S.W. Hwang, A. Sivanantham, I.S. Cho, Solution synthesis and activation of spinel $CuAl_2O_4$ film for solar water-splitting. J. Catal. **400**, 218–227 (2021). https://doi.org/10.1016/j.jcat.2021.06.004
43. Z. Zhang, H. Nagashima, T. Tachikawa, Ultra-narrow depletion layers in a hematite mesocrystal-based photoanode for boosting multihole water oxidation. Angew. Chem. Int. Ed. **59**(23), 9047–9054 (2020). https://doi.org/10.1002/anie.202001919
44. S. Kment, P. Schmuki, Z. Hubicka, L. Machala, R. Kirchgeorg et al., Photoanodes with fully controllable texture: the enhanced water splitting efficiency of thin hematite films exhibiting solely (110) crystal orientation. ACS Nano **9**(7), 7113–7123 (2015). https://doi.org/10.1021/acsnano.5b01740
45. H. Zhang, Y. He, X. Bao, Z. Wang, W. Jiang et al., Fabrication of hematite photoanode consisting of (110)-oriented single crystals. Chemsuschem **16**(19), e202300666 (2023). https://doi.org/10.1002/cssc.202300666
46. Q. Liu, C. Chen, G. Yuan, X. Huang, X. Lü et al., Morphology-controlled α-Fe_2O_3 nanostructures on FTO substrates for photoelectrochemical water oxidation. J. Alloys Compd. **715**, 230–236 (2017). https://doi.org/10.1016/j.jallcom.2017.04.213
47. G. Park, Y.-I. Kim, Y.H. Kim, M. Park, K.Y. Jang et al., Preparation and phase transition of FeOOH nanorods: strain effects on catalytic water oxidation. Nanoscale **9**(14), 4751–4758 (2017). https://doi.org/10.1039/C6NR09790A
48. H. Huang, J. Wang, Y. Liu, M. Zhao, N. Zhang et al., Stacking textured films on lattice-mismatched transparent conducting oxides *via* matched Voronoi cell of oxygen sublattice. Nat. Mater. **23**(3), 383–390 (2024). https://doi.org/10.1038/s41563-023-01746-3
49. Gurudayal, S.Y. Chiam, M.H. Kumar, P.S. Bassi, H.L. Seng et al., Improving the efficiency of hematite nanorods for photoelectrochemical water splitting by doping with manganese. ACS Appl. Mater. Interfaces **6**(8), 5852–5859 (2014). https://doi.org/10.1021/am500643y
50. A.M. Schultz, Y. Zhu, S.A. Bojarski, G.S. Rohrer, P.A. Salvador, Eutaxial growth of hematite Fe_2O_3 films on perovskite $SrTiO_3$ polycrystalline substrates. Thin Solid Films **548**, 220–224 (2013). https://doi.org/10.1016/j.tsf.2013.09.073
51. G. Liu, N. Li, Y. Zhao, M. Wang, R. Yao et al., Porous versus compact hematite nanorod photoanode for high-performance photoelectrochemical water oxidation. ACS Sustain. Chem. Eng. **7**(13), 11377–11385 (2019). https://doi.org/10.1021/acssuschemeng.9b01045
52. K.-Y. Yoon, J. Park, M. Jung, S.-G. Ji, H. Lee et al., NiFeOx decorated Ge-hematite/perovskite for an efficient water splitting system. Nat. Commun. **12**(1), 4309 (2021). https://doi.org/10.1038/s41467-021-24428-7
53. J. López-Sánchez, A. del Campo, S. Román-Sánchez, Ó. Rodríguez de la Fuente, N. Carmona et al., Large two-magnon Raman hysteresis observed in a magnetically uncompensated hematite coating across the morin transition. Coatings **12**(4), 540 (2022). https://doi.org/10.3390/coatings12040540
54. Y. Liu, R.D.L. Smith, Identifying protons trapped in hematite photoanodes through structure-property analysis. Chem. Sci. **11**(4), 1085–1096 (2019). https://doi.org/10.1039/c9sc04853g
55. X. Meng, C. Zhu, X. Wang, Z. Liu, M. Zhu et al., Hierarchical triphase diffusion photoelectrodes for photoelectrochemical gas/liquid flow conversion. Nat. Commun. **14**(1), 2643 (2023). https://doi.org/10.1038/s41467-023-38138-9
56. Y.P. Hou, S.L. Feng, L.M. Dai, Y.M. Zheng, Droplet manipulation on wettable gradient surfaces with micro-/nano-hierarchical structure. Chem. Mater. **28**(11), 3625–3629 (2016). https://doi.org/10.1021/acs.chemmater.6b01544
57. M. Distaso, O. Zhuromskyy, B. Seemann, L. Pflug, M. Mačković et al., Interaction of light with hematite hierarchical structures: experiments and simulations. J. Quant. Spectrosc. Radiat. Transf. **189**, 369–382 (2017). https://doi.org/10.1016/j.jqsrt.2016.12.028
58. S. Tang, W. Qiu, S. Xiao, Y. Tong, S. Yang, Harnessing hierarchical architectures to trap light for efficient photoelectrochemical cells. Energy Environ. Sci. **13**(3), 660–684 (2020). https://doi.org/10.1039/c9ee02986a
59. L. Lyu, X. Hu, S. Lee, W. Fan, G. Kim et al., Oxygen reduction kinetics of Fe–N–C single atom catalysts boosted by pyridinic N vacancy for temperature-adaptive Zn–air batteries. J. Am. Chem. Soc. **146**(7), 4803–4813 (2024). https://doi.org/10.1021/jacs.3c13111
60. L. Lyu, X. Hu, W. Fan, B. Shao, Q. Wang et al., *Operando* hydroxylation of the Sn–co diatomic catalyst boosting ultrastable Zn–air batteries. Nano Lett. **25**(28), 11164–11173 (2025). https://doi.org/10.1021/acs.nanolett.5c02744
61. I. Kwon Jeong, M.A. Mahadik, S. Kim, H.M. Pathan, W.S. Chae et al., Transparent zirconium-doped hematite nanocoral

 https://doi.org/10.1007/s40820-025-02045-z

photoanode *via in situ* diluted hydrothermal approach for efficient solar water splitting. Chem. Eng. J. **390**, 124504 (2020). https://doi.org/10.1016/j.cej.2020.124504

62. J. Kang, K.-Y. Yoon, J.-E. Lee, J. Park, S. Chaule et al., Mesopore generating P doping for efficient photoelectrochemical water splitting. Nano Energy **107**, 108090 (2023). https://doi.org/10.1016/j.nanoen.2022.108090
63. R. Chen, L. Meng, W. Xu, L. Li, Cocatalysts-photoanode interface in photoelectrochemical water splitting: understanding and insights. Small **20**, 2304807 (2024). https://doi.org/10.1002/smll.202304807
64. Z. Zhang, X. Chen, R. Hao, Q. Feng, E. Xie, Van der Waals heterojunction modulated charge collection for H_2O_2 production photocathode. Adv. Funct. Mater. **33**(34), 2303391 (2023). https://doi.org/10.1002/adfm.202303391
65. Y.J. Jeong, D.H. Seo, J.H. Baek, M.J. Kang, B.N. Kim et al., Crystal reconstruction of Mo: $BiVO_4$: improved charge transport for efficient solar water splitting. Adv. Funct. Mater. **32**(52), 2208196 (2022). https://doi.org/10.1002/adfm.202208196
66. H. Wu, L. Zhang, S. Qu, A. Du, J. Tang et al., Polaron-mediated transport in $BiVO_4$ photoanodes for solar water oxidation. ACS Energy Lett. **8**(5), 2177–2184 (2023). https://doi.org/10.1021/acsenergylett.3c00465
67. G. Meng, Z. Chang, L. Zhu, C. Chen, Y. Chen et al., Adsorption site regulations of [W–O]-doped CoP boosting the hydrazine oxidation-coupled hydrogen evolution at elevated current density. Nano-Micro Lett. **15**, 212 (2023). https://doi.org/10.1007/s40820-023-01185-4
68. L. Zhu, J. Huang, G. Meng, T. Wu, C. Chen et al., Active site recovery and N-N bond breakage during hydrazine oxidation boosting the electrochemical hydrogen production. Nat. Commun. **14**(1), 1997 (2023). https://doi.org/10.1038/s41467-023-37618-2
69. S. Li, Y. Hou, L. Jiang, G. Feng, Y. Ge et al., Progress in hydrazine oxidation-assisted hydrogen production. Energy Rev. **4**(1), 100105 (2025). https://doi.org/10.1016/j.enrev.2024.100105